This is the peer reviewd version of the followng article:

Influence of different temperature distributions on the fatigue life of a motorcycle piston / Giacopini, Matteo; Sissa, Simone; Rosi, Roberto; Fantoni, S.. - In: PROCEEDINGS OF THE INSTITUTION OF MECHANICAL ENGINEERS. PART D, JOURNAL OF AUTOMOBILE ENGINEERING. - ISSN 0954-4070. - ELETTRONICO. - 229:9(2015), pp. 1276-1288. [10.1177/0954407014560201]

*Terms of use:*

The terms and conditions for the reuse of this version of the manuscript are specified in the publishing policy. For all terms of use and more information see the publisher's website.

23/04/2026 15:26

(Article begins on next page)

# INFLUENCE OF DIFFERENT TEMPERATURE DISTRIBUTIONS ON THE FATIGUE LIFE OF A MOTORBIKE PISTON

Giacopini, M.[1], Sissa, S.[1], Rosi, R.[1], Fantoni, S.[2]

[1]Department of Engineering "Enzo Ferrari", University of Modena and Reggio Emilia, Modena, Italy

[2]Ducati Motor Holding, Calculation Department, Bologna, Italy

Corresponding author: Matteo Giacopini, Department of Engineering "Enzo Ferrari", University of Modena and Reggio Emilia, Via Vignolese 905, 41125, Modena, Italy, tel. +390592056112, email: matteo.giacopini@unimore.it

**Abstract:** In this paper, Finite Element analyses are performed to evaluate stresses and strains in a motorbike piston. Non-linear Finite Element models are employed to mimic the piston behaviour when subjected to different loading conditions. In particular, gas forces, inertial forces, and piston-to-cylinder contact forces are considered. Proper temperature distributions are applied to the model to include thermal stresses and strains into the analyses. Two different thermal configurations are considered: the first has a standard design of the oil jet hitting the underside zone of the piston crown, while the second one presents modified parameters able to appreciably increase the heat transfer coefficient. The different operating temperature distributions related to the two thermal configurations considered strongly influence the piston thermo-mechanical behaviour. This contribution aims at performing high-cycle fatigue analyses to show how the fatigue life and fatigue-critical points of the component change when moving to the standard configuration to the modified one.

**Keywords:** fatigue, piston, thermal stresses, oil jet

## 1 INTRODUCTION

Piston is one of the most important components in internal combustion engines and at the same time it is one of the most stressed parts of a whole modern vehicle. In fact, pistons have to endure thermo-mechanical cyclic loadings in a wide range of operating conditions, in terms of frequency/amplitude of both temperature and mechanical loading cycles. In the last decades, piston design has been substantially modified and it has been properly rationalised. The ratio between piston diameter and piston height has continuously decreased. Moreover, most of the current pistons do not present a complete skirt, but lateral forces between the piston and the liner are supported by two finite opposite sliding surfaces orthogonal to the con-rod moving plane. This progressive decrease of the piston height and of the circumferential extent of the piston skirt has brought to a consistent reduction of the piston mass, with a consequent decrease of the inertial forces and of the friction losses, with a definite advantage in the fuel consumption reduction.

Thanks to these design improvements and to the high technological materials adopted, pistons are stronger, more durable and lighter. Nevertheless, there are still many different types of damage mechanisms affecting the piston strength, mainly induced by wear, high temperature and fatigue. In particular, fatigue phenomena are recognized to play a crucial role in a large number of piston failures [**1, 2**].

In order to evaluate the mechanical strength of engine components it is necessary to model and to analyse them considering all the possible critical operating conditions. Cyclic stresses and strains, responsible of fatigue phenomena, are essentially related to gas pressure evolution, inertial loads and temperature distribution, so both thermal and mechanical mechanisms are usually involved [**3, 4**].

During the initial stage of the design of a piston, it is difficult to obtain detailed information about its thermal and mechanical behaviour and the piston fatigue life can

be evaluated only with experimental bench tests which are usually excessively costly and time consuming [**5**].

With these preliminary remarks, Finite Element analyses constitute an important tool to be employed to analyse and optimize piston geometries. Nevertheless, only a few numerical studies can be found in the pertinent literature focused on 3-D structural and thermal analyses of engine pistons [**6**].

In [**6]** Finite Element are employed to predict the critical regions where the highest stresses occur, in a spark ignition engine piston made of aluminium alloy. Both thermal and mechanical analyses are presented. Only a single engine thermal configuration is considered and the areas where maxima stresses occur are highlighted. No fatigue results are presented. In [**7**] Finite Element analyses are employed to evaluate the stress and strain distributions in a gasoline engine piston under the coupling effect of thermal loads and combustion pressure. Thermal stresses are recognized to play a crucial role for the piston safety assessment and the authors conclude that it could be useful to decrease the overall piston temperatures in order to decrease the maximum stress. In [**8**] the causes of thermal stress appearance are investigated in order to find out the way to alleviate the maxima stresses in an internal combustion engine piston. Also in this case, thermal strains and stresses are considered to be higher than in other engine parts and they are addressed like the main threat for the piston reliability. The influence of both temperature gradients and piston deformability are investigated. A decrease of the temperature gradients and of the piston stiffness are shown to positively affect the thermo-mechanical behaviour of the piston. In [**9**] the effect of the cooling gallery position on the temperature field and on the thermal stress distribution is investigated for a diesel engine piston. The lowest thermal stresses are registered in the piston when the particular coolant gallery design, able to produce the lowest temperature gradients, is considered.

Recent studies exist about the effect on the engine performance of a thermal barrier coating executed on the top of the piston. For example, in [**5**], both temperature and thermal stress distributions are investigated in a plasmasprayed magnesia-stabilized zirconia coating on an aluminium piston top of a diesel engine. In [**10**], the purpose is to determine the temperature and the stress distributions in a spark ignition engine piston, partially coated with ceramic. In both cases, the focus of the study is the evaluation of the maxima temperatures and of the thermal stress distribution at the interface between the coating and the piston. No results are presented about the influence of the coating on the fatigue life of the piston.

In this contribution, a Finite Element analysis is presented with the aim of evaluating the influence of the temperature distribution on the fatigue life of a motorbike piston. In particular, a first thermal configuration is considered, in which a standard design of the oil jet hitting the underside zone of the piston crown is employed for heat removal purpose. In this case, the piston has experienced different cracks in the piston top and in the upper portion of the pin bosses when subjected to severe bench tests, see Figure 1. Unfortunately, cracks have been observed at a stage of the design process when a massive modification of the piston geometry was no longer allowed. Therefore, it was decided to investigate the effect of a variation of the thermal boundary conditions on the thermo-mechanical behaviour of the piston. In order to decrease the thermal stresses and strains induced by the high temperatures, a second oil jet configuration is introduced in which the geometrical parameters of the jet impinging the underside zone of the piston crown are modified in order to increase the heat transfer coefficient between the oil and the piston, and, consequently, the amount of the heat flux removed by the oil. In fact, a reduction of the maxima temperatures and especially of the temperature gradients is considered to be an effective means for reducing thermal stresses and strains in mechanical component, e.g. [**6-9**]. Surprisingly, for the particular case addressed in this contribution, results show that the modified configuration reduces

the overall maxima temperatures and temperature gradients, but the operating stresses, at least in the critical regions here addressed, increase moving from the original to the modified oil jet configuration. Nevertheless, an improvement in the fatigue life of the component is obtained, and it is essentially related to the higher fatigue properties that the material of the piston exhibits at the lower operating temperatures produced by the modified oil jet.

(a) 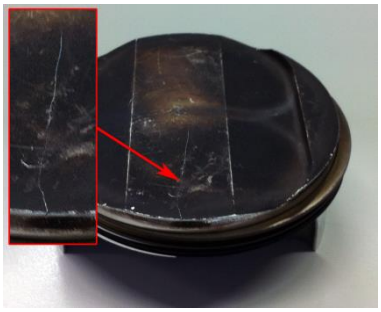 (b) 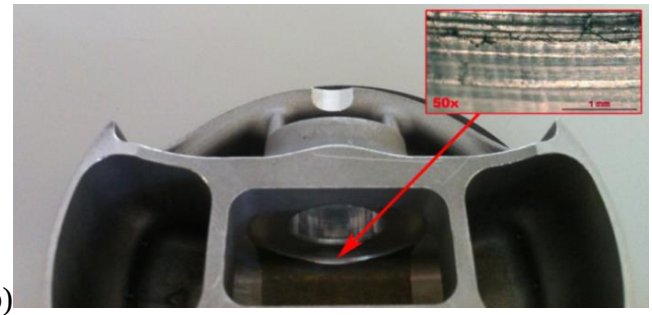


**Figure 1.** Experimentally detected cracks: (a) piston top; (b) upper part of piston bosses.

The present paper is structured as following: a) first of all, the adopted modelling strategy is described; b) then, considering two different cooling oil jet designs, results of thermal analyses are presented aiming at estimating the temperature distribution inside the piston at the most critical operating condition, i.e. maximum power regime; c) results of these thermal analyses are then superposed to the mechanical loads affecting the piston, and stress and strain distributions are calculated; d) finally, results from the mechanical analyses are employed to perform fatigue life estimations of the piston in terms of both safety factor and number of cycles to failure.

## 2 MODELLING STRATEGY

The modelling strategy developed in this study consists in considering separately thermal and mechanical simulations, performed using the commercial Finite Element software MSC.Marc2012®.

Only half the whole components has been modelled, as the piston is symmetrical with respect to the con-rod moving plane. Nevertheless, neither the engine liner nor the engine block are perfectly symmetrical; however, since the piston is the only engine component to be examined, it is felt that a symmetrical modelling is acceptable. Moreover, only the top part of the con-rod has been discretised while its bottom portion has been substituted by rigid elements with the control node positioned in the con-rod big end centre. In particular, former calculations have shown that "cutting" the con-rod at a distance from the small end centre three times greater than the small end inner diameter produces in the piston results that differ less than 1% with respect to those obtained modelling the whole con-rod [**11**]. Figure 2(a) shows all the modelled components.

Particular care has been devoted to the piston meshing process. Second order elements of 1mm size have been adopted for piston top and piston skirt discretization, while a finer mesh with an element size of 0.35mm has been employed in the pin boss area, see Figure 2(b).

Contacts between the different parts have been modelled, see Figure 2(c). In order to correctly detect the interaction between the piston and the others components, clearances have been taken into account between piston and liner and piston and piston pin. In particular, the actual oval/tapered/barrelled piston profile has been modelled [**12**], see Figure 2(d).

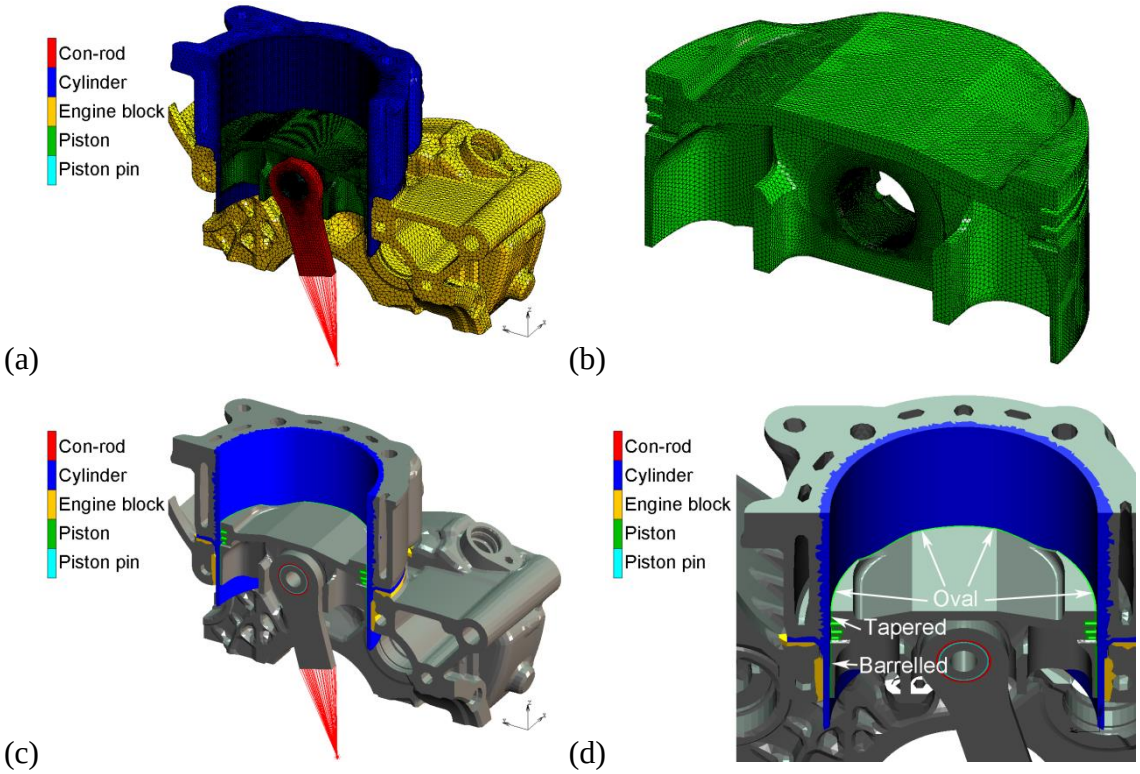


**Figure 2.** Finite Element model: (a) discretized components; (b) piston discretization; (c) contact elements; (d) piston profile.

## 3 THERMAL ANALYSIS

### 3.1 Oil jets configurations

The underside zones of a piston are generally wetted by the oil present in the oil sump and splashed by the crankshaft counterweights rotation. In high performance engines, due to the high thermal loadings involved, an oil jet usually directly hits the underside zone of the piston crown in order to improve the cooling performance while the splash effect only marginally contributes to the heat removal. As a consequence, the heat transfer coefficients in the areas directly hit by the oil jet are greater than the heat transfer coefficients in the other parts where only the convective effect between piston surfaces and the atmosphere present inside the engine crank-case is involved [**13**].

A proper design of the oil jet geometry strongly influences the piston cooling. In particular, the oil jet has to be correctly directed in order to avoid that the particular piston geometry and the relative motion between the piston and the jet prevent the oil from reaching the underside zone of the piston crown where the operating temperature reaches its maximum.

In this contribution, two distinct cooling oil jet configurations are investigated: one has a no-optimized design of the oil jet hitting the underside zone of the piston crown, whereas the other presents modified parameters able to appreciably increase the heat transfer coefficient in this area, see Figure 3. From now on, the two mentioned configurations are denoted as the case A and the case B, respectively.

For case A: in the first case addressed in this paper, a former oil jet configuration is considered. In particular, the jet is characterized by a small nozzle able to direct the oil in the underside part of the piston. Unfortunately, the peculiar geometry of the piston and in particular the transversal ribs between the piston bosses and the piston skirt, prevent the oil from reaching the center of the area for most of the operating cycle, see Figure 3.

For case B: Alternatively, a second jet configuration has been proposed with a modified “S-shaped” nozzle. In this case, the oil directly hits the underside surface of the piston near the center where the highest temperatures exist.

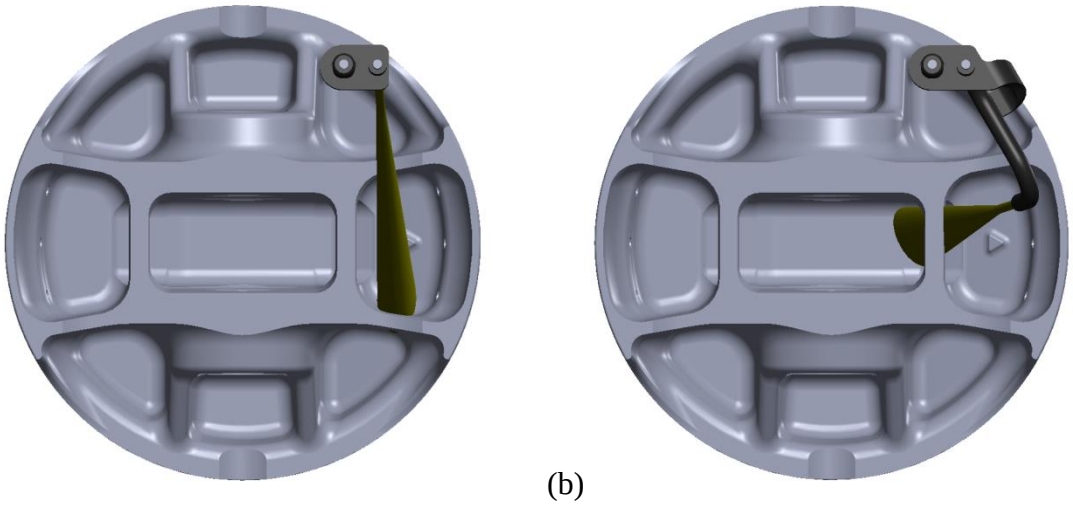

(a) (b)

**Figure 3.** Cooling oil jet hitting the underside piston crown: (a) original oil jet; (b) modified oil jet.

### 3.2 Boundary conditions

In the following, the boundary conditions applied to the thermal model are described. The methodology employed is the same as the one described in [**14**] and it is briefly recalled in the following for the sake of clarity.

***Piston top.*** The results from a previous CFD-3D simulation of the combustion process, from which the gas temperatures and the corresponding heat transfer coefficients are derived [**14**], are employed as external boundary conditions and they are applied to the top surface of the piston. In particular, the maximum power operating condition has been considered, since it produces the most severe thermal loading and maxima temperatures inside engine components [**4**].

It is well known that temperature oscillations can be observed at the walls facing the combustion chamber [**15**]. Nevertheless, because of the relevant thermal inertia of the metal components, these temperature oscillations due to the instantaneous heat flux variation are expected to moderately affect the thermo-structural behaviour of the piston

[**7**]. Therefore, instantaneous heat transfer coefficients and gas temperatures deriving from the CFD combustion simulations can be averaged through a single thermodynamic cycle of the engine, e.g. [**4**, **16**], see Figure 4.

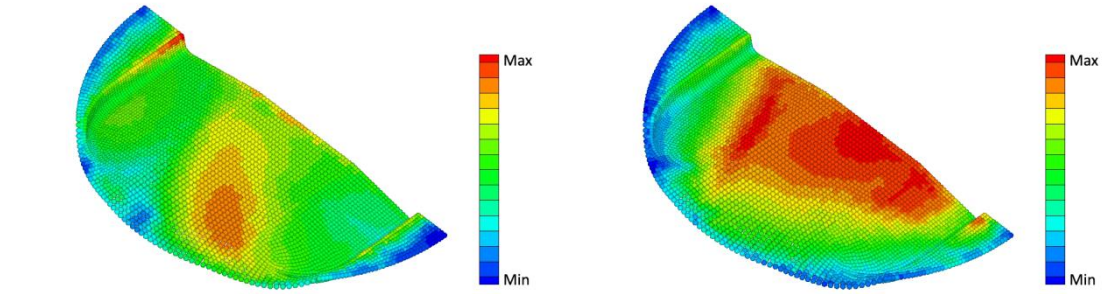


(a) (b)

**Figure 4.** Boundary conditions applied to the piston top surface: (a) heat transfer coefficients; (b) gas temperatures.

Once the boundary conditions applied to the upper surface of the piston have been defined, the thermal energy exchanged by the piston with the other components and with the oil has to be estimated in order to solve the problem of the thermal diffusion inside the piston.

Starting from literature results [**16**–**21**], various formulae have been identified, of both analytical and empirical derivation. By this way, the different heat transfer coefficients have been estimated in terms of various engine parameters.

As a consequence, the piston has been subdivided into a certain number of zones and proper values of heat transfer coefficients and reference temperatures have been applied to each zone.

***Piston rings and piston skirt.*** The thermal circuit method [**16**] has been employed to mimic the heat transfer mechanism in the regions of the piston rings and piston skirt, see Figure 5, where:

- R1: conductive oil film resistance;
- R2: conductive liner resistance;
- R3: convective water-jacket resistance.

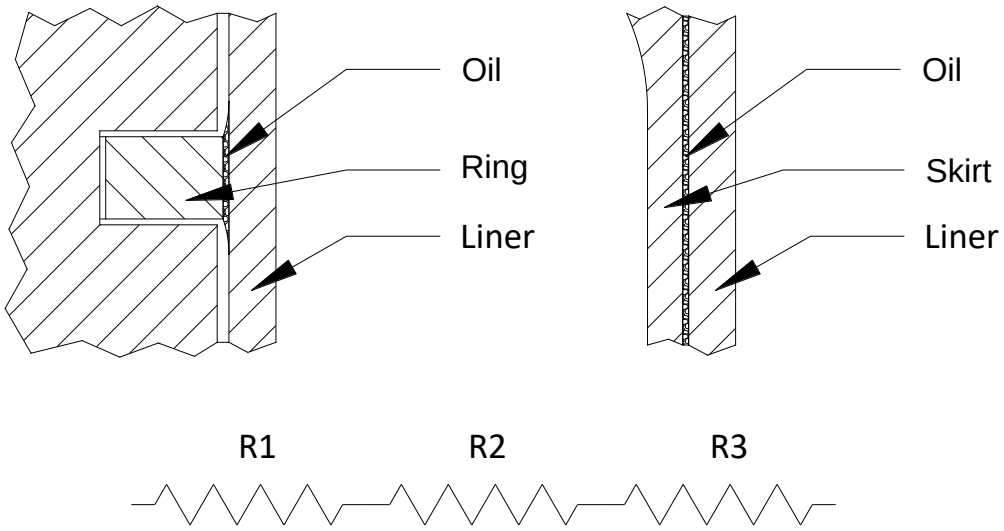


**Figure 5.** Thermal resistance model for rings and skirt.

The effective heat transfer coefficients are obtained from:

$$h_{eff} = \frac{1}{R_{tot} A_{eff}} \tag{1}$$

where $R_{tot}$ is the total resistance and $A_{eff}$ is the effective contact area between the rings and the liner and the skirt and the liner.

***Oil jet.*** Many empirical, semi-analytical and numerical models are available for the evaluation of the heat transfer coefficients for jets of fluid impinging generic surfaces [**22**, **23**]. In particular, the experimental correlation given in [**24**] has been successfully

employed in [**13**] for the investigation of the piston cooling using oil jets in heavy duty diesel engines, and it has been recently validated versus numerical CFD results in [**25**]. This correlation for the local heat transfer coefficient at the piston underside surfaces as a function of the radial distance from the stagnation point, *r*, is given by:

$$h(r) = \mathrm{Nu}\frac{k}{d} = \mathrm{Nu}_0\left[1 + f\left(\frac{r}{d}\right)^{-9}\right]^{\frac{-1}{9}}\frac{k}{d} \tag{2}$$

where *k* is the oil thermal conductivity, *d* is the jet diameter, $\mathrm{Nu}_0$ is stagnation point Nusselt number expressed by:

$$\mathrm{Nu}_0 = 2.67\,\mathrm{Re}^{0.567}\ \ \mathrm{Pr}^{0.4}\left(\frac{z}{d}\right)^{-0.0336}\left(\frac{v}{d}\right)^{-0.237} \tag{3}$$

with *z* the distance of the stagnation point from the nozzle and *v* the jet velocity, and

$$f\left(\frac{r}{d}\right) = a\mathrm{e}^{b\left(\frac{r}{d}\right)} \tag{4}$$

Values of the constants *a* and *b* of equation (4) are functions of the nozzle diameter *d* and listed in Table 1.

**Table 1.** Correlation coefficients for equation (4) [**24**].

| *d* [mm] | *a* | *b* |
|---|---|---|
| 2.2 | 1.15 | -0.23 |
| 4.1 | 1.34 | -0.41 |
| 5.8 | 1.48 | -0.56 |
| 8.9 | 1.57 | -0.7 |

In this paper this same correlation has been adopted for the evaluation of the heat transfer coefficients in the areas of the back side of the piston crown directly impinged by the oil jet. Instantaneous heat transfer coefficients have been averaged considering a single engine cycle. Figure 6 depicts the heat transfer coefficient distributions in the different areas interested by the jet impingement for the two configurations investigated.

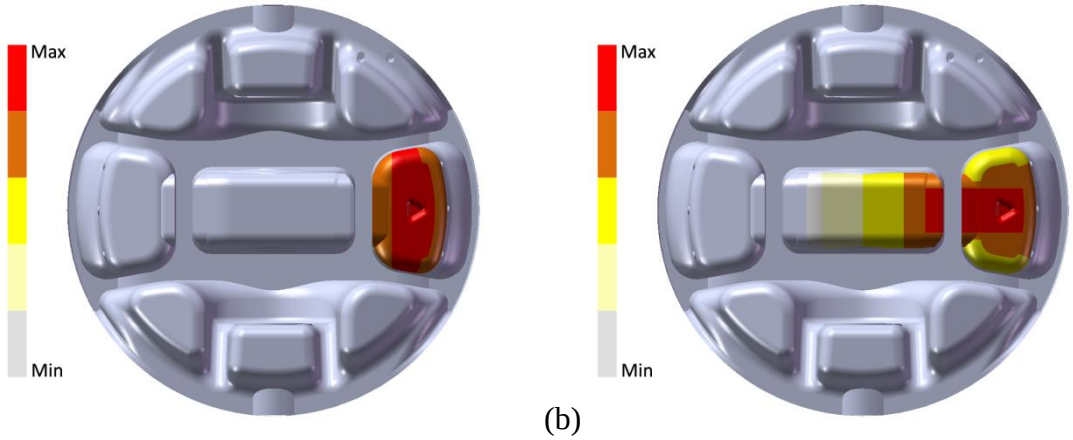


(a) (b)

**Figure 6.** Heat transfer coefficients in the surfaces directly hit by the oil: (a) original oil jet; (b) modified oil jet.

***Underside/inside of the piston.*** In the underside zones of the piston crown and in the inner zones of the piston skirt not directly impinged by the jet, the heat transfer coefficients between the piston and the atmosphere into the engine crank-case can be up to one order of magnitude lower than the ones evaluated for the surfaces directly impinged by the jet [**20**, **21**]. In this paper, the same empirical correlations adopted in [**16**] both for horizontal, equation (5), and vertical, equation (6), surfaces have been employed:

$$h = 900\left(\frac{n}{4600}\right)^{0.35} \quad (5)$$

$$h = 240\left(\frac{n}{4600}\right)^{0.35} \quad (6)$$

where $n$ is the engine revving speed expressed in rev/min.

### 3.3 Thermal properties of the materials employed

Table 2 collects the material considered for each modelled component and the corresponding thermal properties adopted for the thermal analyses.

**Table 2.** Thermal properties of the materials employed for the thermal analyses.

| Component | Material | Thermal conductivity [W/m$^2$.K] |
|---|---|---|
| Piston | Aluminum alloy AA2618 | 146 |
| Cylinder | Aluminum alloy AlSi10Mg | 155 |
| Engine block | Aluminum alloy AlSi7MgTi | 135 |
| Piston pin | Steel 33CrMoV12 | 39 |
| Con-rod | Steel 38NiCrMo4 | 52 |

### 3.4 Results

Figure 7 shows the temperature distributions obtained within the piston with the two different oil jet configurations considered. As expected, both the maximum temperature on the piston top and the temperature gradient computed along the cylinder axis of the case A are higher than the ones of the case B.

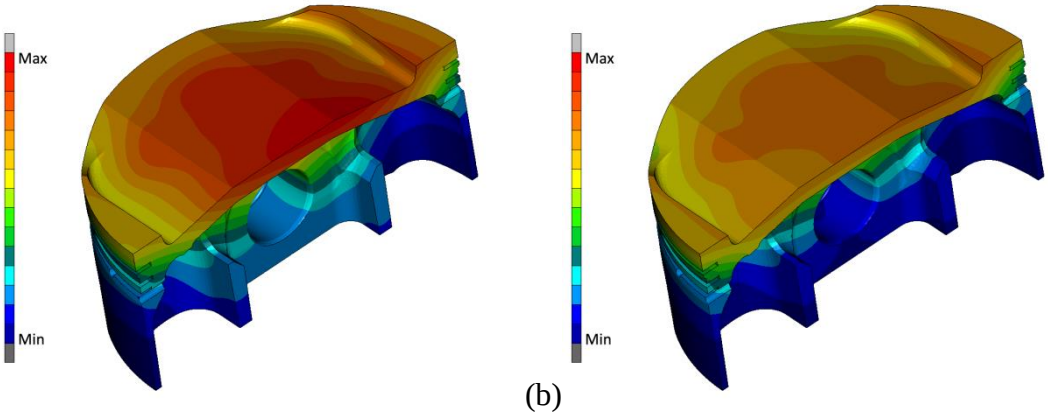


(a) (b)

**Figure 7.** Temperature distribution within the piston: (a) original oil jet; (b) modified oil jet.

In particular, numerical forecasts show a 12% decrease of the maximum temperature and a 21% decrease of the gradient along the cylinder axis.

Results of the thermal analysis have been qualitatively validated versus experimental residual Brinell hardness measurements, performed at the centre of the piston top after full power long runs of the engine, e.g. [**14**]. With the modified oil jet configuration, a 18% increase of the residual hardness value has been detected, with respect to the standard oil jet configuration.

Focusing on the piston top, the modified oil jet reduces the maxima global temperatures, but it also modifies the radial temperature gradient. In fact, the maximum temperature in the case A occurs at the piston top centre, while in the case B, thanks to the higher amount of heat flux removed from the centre of the underside zone of the piston crown by the modified oil jet, the maximum temperature area expands toward the piston top periphery, see Figure 7.

## 4 MECHANICAL ANALYSIS

### 4.1 Model description

Time independent mechanical analyses have been performed in which the mechanical boundary conditions have been superposed to the previously calculated temperature fields.

Five different load configurations have been considered. In particular, piston, piston pin and con-rod have been correctly positioned according to different engine operating points representing the most critical conditions that the piston experiences during a complete engine cycle:

- maximum gas pressure (near top dead centre during the combustion phase);
- top dead centre at the beginning of the induction stroke;
- bottom dead centre;
- maximum lateral force during the expansion phase;
- maximum lateral force during the compression phase.

All the simulations have been performed considering the maximum power regime. Table 3 collects the main engine data employed for the analysis.

**Table 3.** Main engine data.

| | | |
|---|---|---|
| Displacement | 1198 | $cm^3$ |
| Number of cylinders | 2 | |
| Bore | 106 | mm |
| Stroke | 67.9 | mm |
| Con-rod length | 124 | mm |
| Compression ratio | 12.8 | |
| Maximum revving speed | 11000 | rpm |

### 4.2 Boundary conditions

The temperature fields evaluated in the previously described thermal analyses have been employed as external thermal boundary conditions in the mechanical models.

Moreover, different mechanical loads have been superposed to the thermal loads depending on the piston position during the operating cycle. In particular, the alternating inertial acceleration has been evaluated as a function of the crank angle, $\theta$, by the classical formula:

$$a(\theta) = \varpi^2 r \left(\cos\vartheta + \lambda \cos 2\theta\right) \tag{7}$$

where $\varpi$ is the angular velocity, $r$ is the crank radius and $\lambda$ is the crank radius to con-rod length ratio, see Figure 8(a). The inertial acceleration has been applied to all the elements of the model, considering that the portion of con-rod that has been modelled approximately corresponds to its reciprocating part. The combustion gas pressure, acting on the piston top surface, has been evaluated via a CFD-1D model of the whole engine and validated versus experimental data obtained during bench tests of the engine equipped with a spark plug combustion pressure sensor, see Figure 8(b). Both acceleration and gas pressure have been one-degree crankshaft angle step sampled, and the corresponding values have been employed for the different piston positions considered, see Table 4.

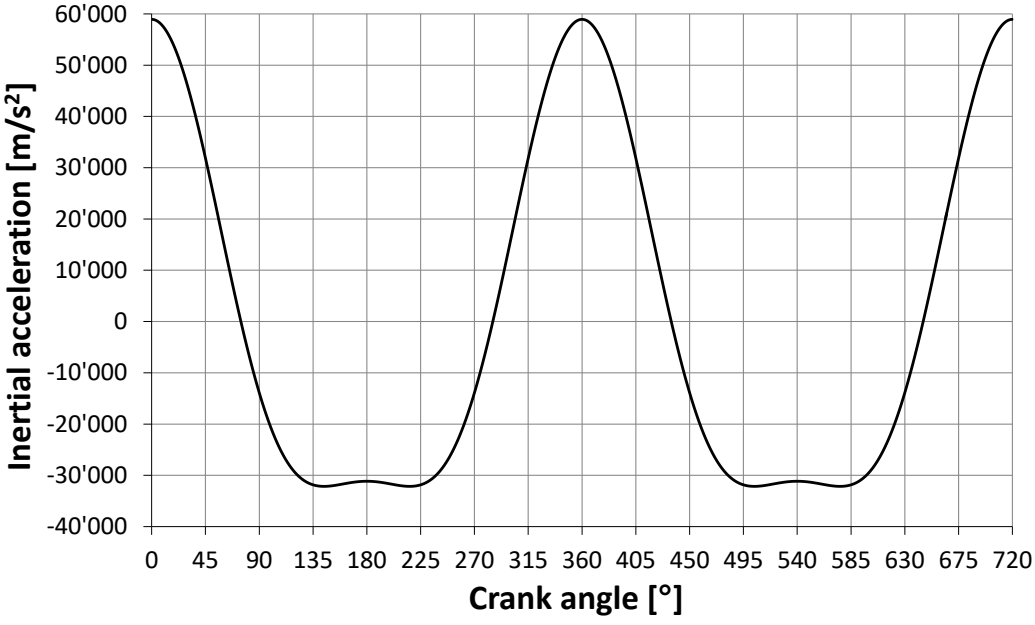


(a)

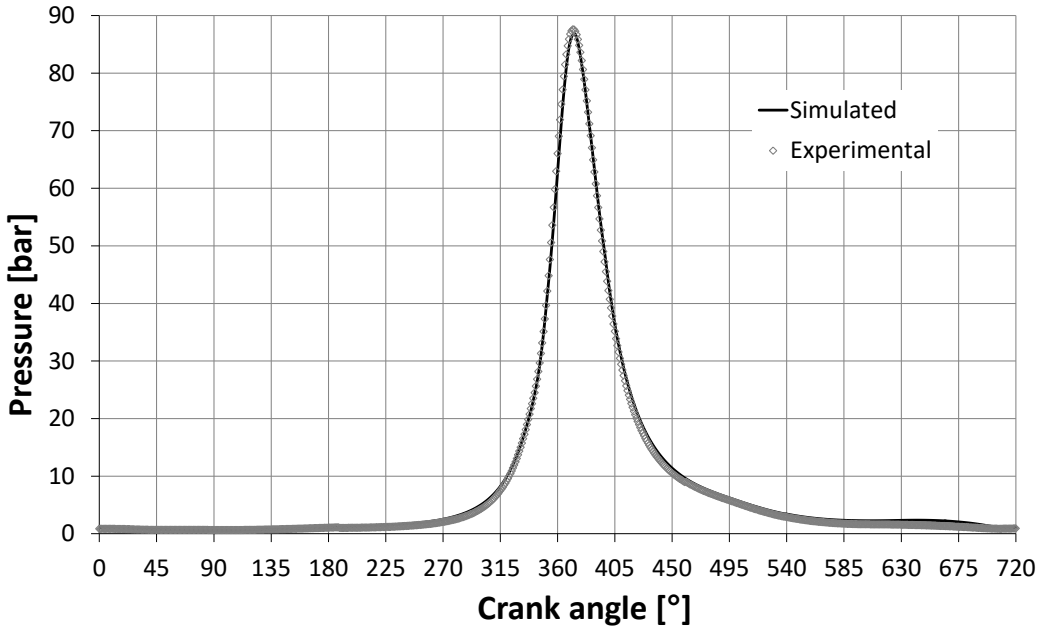


(b)

**Figure 8.** Mechanical loadings: (a) inertial alternating acceleration; (b) gas pressure.

**Table 4.** Boundary conditions for the different load cases considered.

| Load case | Crank angle [°] | Acceleration [m/s$^2$] | Gas pressure [bar] |
|---|---|---|---|
| Maximum gas pressure | 373 | 56380 | 86.8 |
| Top dead centre during the beginning of the induction stroke | 0 | 58940 | 0.94 |
| Bottom dead centre | 540 | -31158 | 3.42 |
| Maximum lateral force during the expansion phase | 472 | -26868 | 8.19 |
| Maximum lateral force during the compression phase | 243 | -28617 | 1.74 |

### 4.3 Mechanical properties of the materials employed

Table 5 collects the material considered for each modelled component and the corresponding mechanical properties adopted for the mechanical analyses.

**Table 5.** Mechanical properties of the materials employed for the mechanical analyses.

| Component | Material | Young's modulus [MPa] | Density [kg/dm$^3$] | Expansion coefficient [m/m.°C] |
|---|---|---|---|---|
| Piston | Aluminum alloy AA2618 | 74000 | 2.7 | $2.2 \times 10^{-6}$ |
| Cylinder | Aluminum alloy AlSi10Mg | 74500 | 2.7 | $2.2 \times 10^{-6}$ |
| Engine Block | Aluminum alloy AlSi7MgTi | 74000 | 2.7 | $2.2 \times 10^{-6}$ |
| Piston Pin | Steel 33CrMoV12 | 210000 | 7.8 | $1.2 \times 10^{-6}$ |
| Con-rod | Steel 38NiCrMo4 | 210000 | 7.8 | $1.1 \times 10^{-6}$ |

All the analyses have been performed considering elastic materials, apart from the piston material for which the elasto-plastic behaviour has been taken into account with properties varying with temperature. Details about the piston material are given in the following.

***Piston material static properties.*** The material employed for the piston manufacturing is a T6 treated AA2618 aluminium alloy. The non-linear material behaviour has been considered to carry out plastic strains by the numerical simulations. In particular, the Chaboche [**26**, **27**] stress-strain relationship has been used, based on the non-linear kinematic hardening rule expressed by:

$$X\left(\varepsilon_{\mathrm{p}}\right)=\alpha\frac{K}{\gamma}-\left(X_{0}-\alpha\frac{K}{\gamma}\right)\mathrm{e}^{-\alpha\gamma\left(\varepsilon_{0}-\varepsilon_{\mathrm{p}}\right)} \tag{8}$$

where $\alpha$ = sign($\sigma - X$), $K$ and $\gamma$ are experimentally determined material properties depending on temperature and $\varepsilon_{\mathrm{p}}$ is the local plastic strain. In particular, the constants $K$ and $\gamma$ have been tuned versus experimental results obtained for "as forged" test specimens at the different temperatures of 20°C, 100°C, 200°C, 250°C and 300°C. "Fully aged" parameters have then been extrapolated considering data of [**28**]. Table 6 collects the different values of the material static parameters employed in the analyses.

**Table 6.** Piston material static parameters as functions of the temperature.

| Temperature | Young's modulus | "As forged" Chaboche parameters | | | "Fully aged" Chaboche parameters | | |
|---|---|---|---|---|---|---|---|
| T [°C] | $E$ [MPa] | Yield stress, $R$s [MPa] | $K$ | $\gamma$ | Yield stress, $R$s [MPa] | $K$ | $\gamma$ |
| 20 | 74000 | 321 | 7403 | 45.3 | 321 | 7403 | 45.3 |
| 100 | 72000 | 311 | 5922 | 46.7 | 311 | 5922 | 46.7 |
| 200 | 68200 | 306 | 4313 | 48.6 | 228 | 2772 | 49.3 |
| 250 | 65500 | 237 | 650 | 53.2 | 111 | 244 | 53.5 |
| 300 | 62000 | 147 | 266 | 53.6 | 54 | 90 | 53.7 |

Figure 9 depicts experimental end numerical stress-plastic strain curves as functions of the temperature.

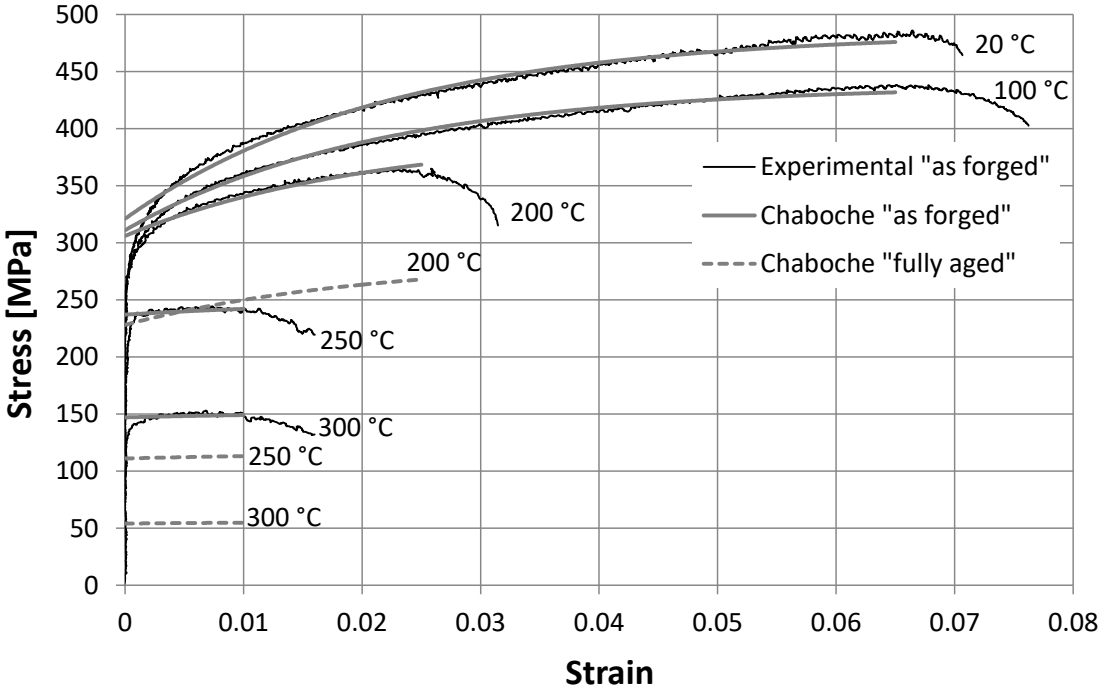


**Figure 9.** Experimental and numerical stress-plastic strain curves as functions of the temperature.

***Piston material fatigue properties.*** Two different fatigue criteria have been adopted in the analyses:

- the Dang Van criterion [**29**, **30**] which is a stress-based multiaxial criterion employed to compute a fatigue safety factor taking into account a certain load history;
- the Brown-Miller criterion [**31**] which is a strain-based multiaxial criterion capable to estimate the number of cycles to failure. In this case, the general load history is elaborated with a rainflow algorithm to obtain a discrete number of equivalent fatigue cycles [**32**, **33**].

The material fatigue limits to be employed in the Dang Van criterion have been derived from Wöhler temperature dependent curves considering the maximum alternating stress at $10^8$ cycles [**34**]. This number of cycles has been conventionally assumed as a reference value for the reason that aluminium alloys do not exhibit a perfectly horizontal asymptote in the Wöhler diagram.

For the Brown-Miller criterion, Manson-Coffin constants of equation (9) have to be defined as functions of the temperature:

$$\frac{\Delta\varepsilon}{2}=\frac{\Delta\varepsilon_{\mathrm{e}}}{2}+\frac{\Delta\varepsilon_{\mathrm{p}}}{2}=\frac{\sigma_{\mathrm{f}}^{'}}{E}\left(2N\right)^{b}+\varepsilon_{\mathrm{f}}^{'}\left(2N\right)^{c} \tag{9}$$

In this paper, the constants have been derived following the statistical predictions proposed in [**35**]. In particular, low-cycle fatigue parameters $\varepsilon_{\mathrm{f}}^{'}$ and $c$ have been assumed as temperature independent and they have been extracted from the experimental results of [**36**] valid for a defined temperature of 200°C, while high-cycle fatigue parameters $\sigma_{\mathrm{f}}^{'}$ and $b$ have been then fitted versus experimental results of [**34**] for other temperature values, namely 20, 150, 260 and 315°C. Table 7 collects the different values of the material fatigue parameters employed in the analyses

**Table 7.** Piston material fatigue parameters as functions of the temperature.

| Temperature [°C] | Fatigue limit [MPa] | Young's Modulus $E$ [MPa] | Fatigue ductility coefficient $\varepsilon_{\mathrm{f}}^{'}$ | Fatigue ductility exponent $c$ | Fatigue strength coefficient $\sigma_{\mathrm{f}}^{'}$ [MPa] | Fatigue strength exponent $b$ |
|---|---|---|---|---|---|---|
| 20 | 123 | 74000 | 0.55 | -0.96 | 598 | -0.083 |
| 150 | 100 | 70000 | 0.55 | -0.96 | 638 | -0.097 |
| 200 | 82 | 68200 | 0.55 | -0.96 | 697 | -0.112 |
| 260 | 65 | 64000 | 0.55 | -0.96 | 729 | -0.1265 |
| 315 | 49 | 61000 | 0.55 | -0.96 | 682 | -0.1378 |

Figure 10 depicts experimental end numerical ε-N curves as functions of the temperature.

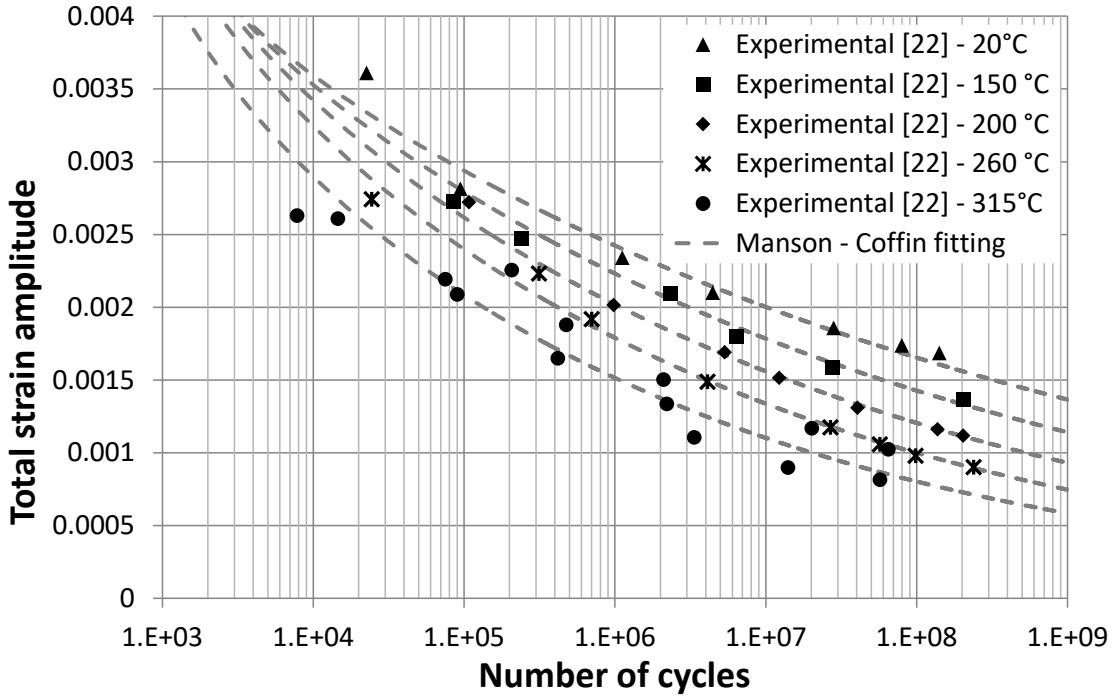


**Figure 10.** Experimental and numerical ε-N curves as functions of the temperature.

### 4.4 Results

For both the cases A and B, the highest stress values arise inside the piston when it is at top dead centre during the combustion phase. Nevertheless, comparing results of the case A and B, the piston mechanical behaviour is far from expectations. In fact, the stresses evaluated inside the piston in the most critical areas in the case A are lower than those calculated in the case B, see Figure 11 and Figure 12. In particular a 18% increase is registered in the value of the von Mises stress on the piston top and a 30% increase on the upper part of the piston bosses moving from the original oil jet configuration to the modified one.

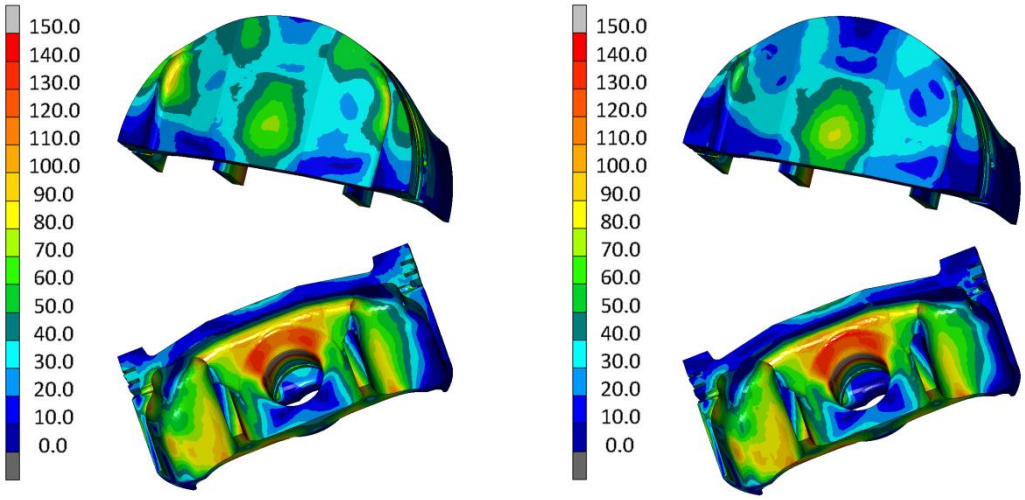


(a) (b)

**Figure 11.** Comparison of equivalent von Mises stress: (a) original oil jet; (b) modified oil jet.

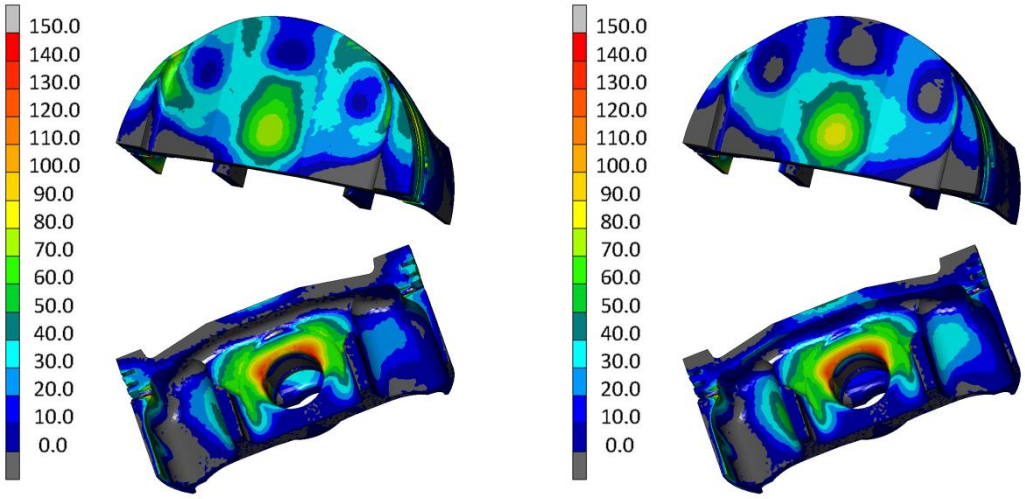


(a) (b)

**Figure 12.** Comparison of principal stress max: (a) original oil jet; (b) modified oil jet.

This unexpected result may be rationalized by considering the thermal deformation induced by the different temperature fields of the two cases A and B investigated. In particular, in the case B the modified oil jet impinging the underside zone of the piston crown produces a lower temperature in the central area of the piston top while, on the contrary, in the case A, the central portion of the piston top exhibits the highest temperatures and it tends to expand more than the peripheral counterpart. Therefore, only in this case, a compressive state arises in the top central portion of the piston that helps reduce the operating stresses in this zone. Figure 13 confirms this explanation. In fact, if only thermal stresses are analysed, a higher compressive state arises in the top central part of the piston when results of the case A are considered.

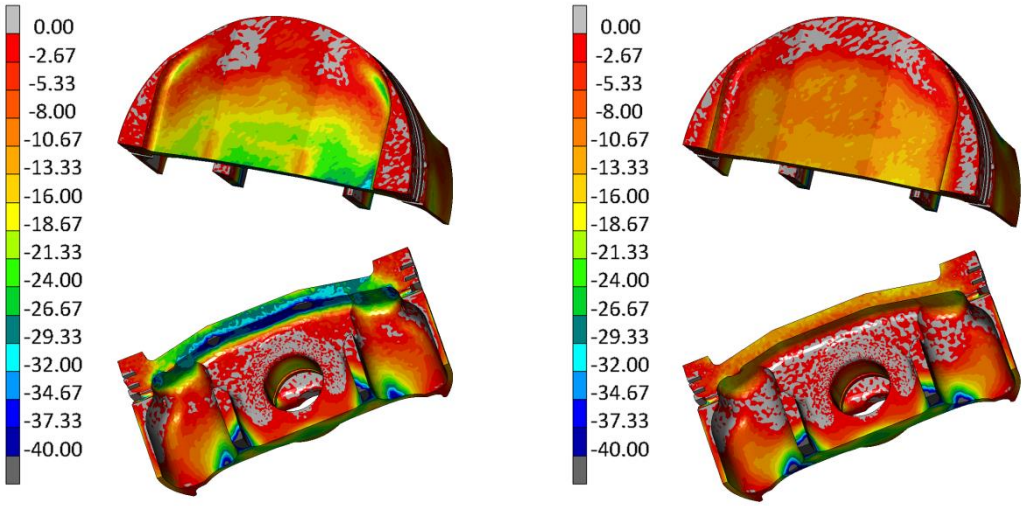


(a) (b)

**Figure 13.** Comparison of thermal principal stress min: (a) original oil jet; (b) modified oil jet.

## 5 FATIGUE ANALYSIS

The superposition of thermal and mechanical loadings can promote both high cycle and low cycle fatigue phenomena [**1**, **4**]. In this case, as no plastic strains have been registered at the end of all the numerical simulations performed even when "fully aged" material properties have been considered, only high cycle fatigue has been taken into account. In particular, considering the experimental cracks observed during severe bench tests, the upper part of the piston bosses and the piston top have been investigated in detail, see Figure 1.

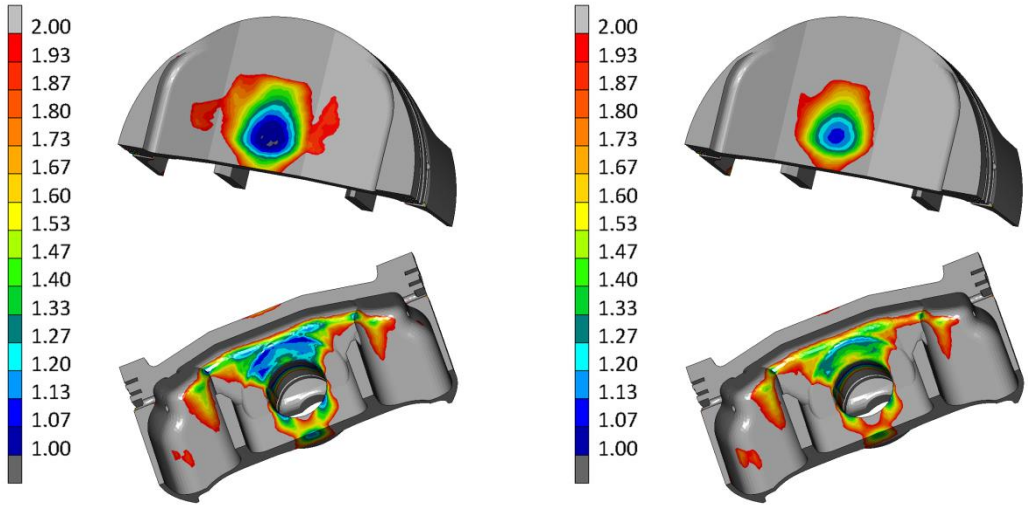


(a) (b)

**Figure 14.** Dang Van safety factors: (a) original oil jet; (b) modified oil jet.

Figure 14 shows a comparison between the Dang Van safety factors calculated for the case A and B. In particular, results from the case A exhibit lower fatigue safety factors than those from the case B. This fact is essentially due to the drop of the fatigue properties of the material at high temperatures as the highest stresses in the case A are lower than those in the case B (see data of Table 7 and Figure 10).

Figure 15 shows the results in terms of Brown-Miller number of cycles to failure for the two oil jet configurations considered. Results confirm the previous ones, and the minima numbers of cycles to failure are detected for the case A.

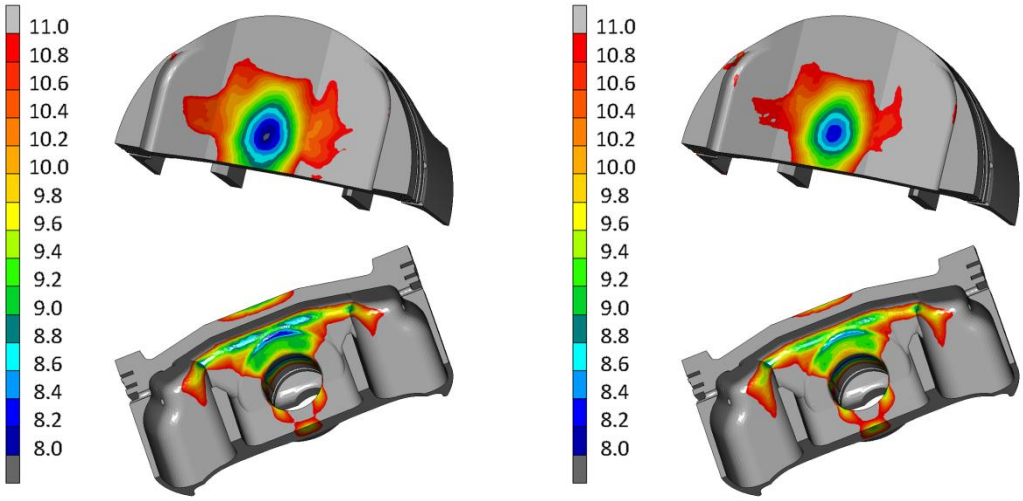


(a) (b)

**Figure 15.** Brown-Miller number of cycles to failure – log of life: (a) original oil jet; (b) modified oil jet.

A comparison of the results of Figure 14 and Figure 15 with the experimental cracks of Figure 1 confirms that the proposed methodology correctly estimates the fatigue strength of the piston analysed. In fact, both the location of minima Dang Van safety factors and minima Brown-Miller numbers of cycles to failure correspond to effective crack initiation points.

## 6 CONCLUSION

In this contribution, non-linear Finite Element analyses have been performed to evaluate stresses and strains in a motorbike piston, subjected to both thermal and mechanical loads.

In particular, two different oil jet configurations have been considered: one has a standard oil jet hitting the underside zone of the piston crown, while the other presents modified parameters able to reduce the thermal load of the piston. This aspect clearly influences the thermo-mechanical behaviour of the piston. Surprisingly, the higher stresses have been registered for the modified oil jet configuration, at least for the critical regions addressed in this contribution.

Fatigue calculations have been then performed. High cycle fatigue results underline how an improved oil jet allows a better fatigue behaviour of the piston to be achieved. This result is essentially related to the decrease of the temperatures inside the piston and to the consequent increase of the mechanical properties of the material at the corresponding operating condition when an improved oil jet is employed.

Thermal low cycle fatigue phenomena do not significantly affect the piston in both the two oil jet configuration considered since no plastic strains arise in the piston top due to both thermal and mechanical loads.

## REFERENCES

**1 Silva, F. S.** Fatigue on engine pistons – A compendium of case studies. *Eng. Fail. Anal.*, 2006, **13**, 480–492.

**2 Floweday, G., Petrov, S., Tai, R. B.** and **Press, J.** Thermo-mechanical fatigue damage and failure of modern high performance diesel pistons. *Eng. Fail. Anal.*, 2011, **18**, 1664–1674.

**3 Lederer, G., Charkaluk, E., Verger, L.,** and **Constantinescu, A.** Numerical Lifetime Assessment of Engine Parts Submitted to Thermomechanical Fatigue, Application to Exhaust Manifold Design. SAE Technical Paper 2000-01-0789, 2000.

**4 Fontanesi, S.** and **Giacopini, M.** Multiphase CFD-CHT optimization of the cooling jacket and FEM analysis of the engine head of a V6 diesel engine. *Appl. Therm. Eng.*, 2013, **52**(2) , 293–303.

**5 Cerit, M.** and **Coban, M.** Temperature and thermal stress analyses of a ceramic-coated aluminum alloy piston used in a diesel engine. *Int. J. Therm. Sci.*, 2014, **77**, 11–18.

**6 Calbureanu, M. X., Malciu, R., Tutunea, D., Ionescu, A.** and **Lungu, M.** The finite element analysis of the thermal stress distribution of a piston head. *Int. J. Mech.*, 2013, **7**(4), 467–474.

**7 Hongyuan, Z., Zhaoxun, L.** and **Dawei, X.** An analysis to thermal load and mechanical load coupling of a gasoline engine piston. *J. Theor. Appl. Inf. Tech.*, 2013, **48**(2), 911–917.

**8 Zhang, Y. M., Zhang, W. Z.** and **Cao, Y. F.** Study on alleviating thermal stress of piston head. *Appl. Mech. Mater.*, 2012, **271–272**, 227–231.

**9 Liu, J. X., Wang, Y.** and **Zhang, W. Z.** The effects of the cooling gallery position on the piston temperature field and thermal stress. *Appl. Mech. Mater.*, 2010, **37–38**, 1462–1465.

**10 Cerit, M.** Thermo mechanical analysis of a partially ceramic coated piston used in an SI engine. *Surf. Coat. Tech.*, 2011, **205**, 3499–3505.

**11 Rubino, D.** Sviluppo di un modello di calcolo del danneggiamento di componenti di motori ad alta potenza specifica, (Development of a numerical methodology for the damage assessment of high performance engine components), Master Thesis, Vehicle Engineering, Department of Mechanical Engineering “Enzo Ferrari”, University of Modena and Reggio Emilia, 2012, (in Italian).

**12 Mahle GmbH**, Pistons and engine testing, ATZ/MTZ-Fachbuch, Springer Vieweg, Wiesbaden, Germany, 2012.

**13 Agarwal, A. K.** and **Varghese, M. B.** Numerical investigations of piston cooling using oil jet in heavy duty diesel engines. *Int. J. Engine Res.*, 2006, **7**, 411–421.

**14 Cantore, G., Giacopini, M., Rosi, R., Strozzi, A., Pelloni, P., Forte, C., Achiluzzi, M., Bianchi, G. M., Ceschini, L.** and **Morri, A.** Validation of a combined CFD/FEM methodology for the evaluation of thermal load acting on aluminum alloy pistons through hardness measurements in internal combustion engines. *Metall. Sci. Technol.*, 2011, **29**, 16-25.

**15 Rakopoulos, C.D., Rakopoulos, D.C., Mavropoulos, G.C.** and **Giakoumis, E.G.** Experimental and theoretical study of the short term response temperature transients in the cylinder walls of a diesel engine at various operating conditions. *Appl. Thermal Eng.*, 2004, 24, 679–702.

**16 Esfahanian, V., Javaheri, A.** and **Ghaffarpour, M.** Thermal analysis of an SI engine piston using different combustion boundary condition treatments. *Appl. Therm. Eng.*, 2006, **26**, 277–287.

**17 Rakopoulos, C., Mavropoulos, G., and Hountalas, D.** Modeling the Structural Thermal Response of an Air-Cooled Diesel Engine under Transient Operation Including a Detailed Thermodynamic Description of Boundary Conditions, SAE paper 981024, 1998.

**18 Liu, Y.** and **Reitz, R.D.** Multidimensional modeling of combustion chamber surface temperatures. SAE paper 971539, 1997.

**19 Liu, Y.** and **Reitz, R.D.** Modeling of heat conduction within chamber walls for multidimensional internal combustion engine simulations. *Int. J. Heat Mass Tran.*, 1988, **41(**6/7), 859–869.

**20 Stotter, A.** Heat transfer in piston cooling. SAE paper 660757, 1966.

**21 French, C. C. J.** Piston cooling. SAE paper 720024, 1972.

**22 Down, S. J.** and **James, E. H.** Jet impingement heat transfer – a literature survey. ASME paper 87-HT-35, 1987.

**23 Jambunathan, K., Lai, E., Moss, M. A.** and **Button, B. L.** A review of heat transfer data for single circular jet impingement. *Int. J. Heat Fluid Fl.*, 1992, **13**, 106–115.

**24 Stevens, J.** and **Webb, B. W.** Local heat transfer coefficient under an axisymmetric, single-phase liquid jet. *J. Heat Trans.-T. ASME*, 1991, **113**, 71–78.

**25 Najafabadi, M. I., Mirsalim, M., Hosseini, V.** and **Alaviyoun, S.** Experimental and numerical study of piston thermal management using piston cooling jet. *J. Mech. Sci. Technol.*, 2014, **28**(3), 1079–1087.

**26 Chaboche, J. L.** Time-Independent constitutive theory for cyclic plasticity. *Int. J. Plasticity*, 1986, **2**, 149–188.

**27 Chaboche, J. L.** Constitutive equations for cyclic plasticity and cyclic viscoplasicity. *Int. J. Plasticity*, 1989, **5**, 247–302.

**28 Kaufman, J. G.** *Properties of aluminum alloys: tensile, creep, and fatigue data at high and low temperatures*, 2006 (ASM International, Novelty, OH)

**29 Dang Van, K., Cailletaud, G., Flavenot, J.F., Le Douaron, A.** and **Lieurade, H.P.** Criterion for high-cycle fatigue failure under multiaxial loading, in: M.W. Brown, K.J. Miller (Eds.), Biaxial and Multiaxial Fatigue, EGF 3, Mechanical Engineering Publications, London, 1989, pp. 459-478.

**30 Dang Van, K., Griveau, B.** and **Message, O.** On a new multiaxial fatigue limit criterion: theory and application, in: M.W. Brown, K.J. Miller (Eds.), Biaxial and Multiaxial Fatigue, EGF 3, Mechanical Engineering Publications, London, 1989, pp. 479-496.

**31 Brown, M.W.** and **Miller, K.J.** A theory for fatigue failure under multiaxial stress-strain conditions. *Proc. Inst. Mech. Engrs.*, 1973, **187**, 745–755.

**32 Matsuishi, M.** and **Endo, T.** Fatigue of metals subjected to varying stress. Fukuoka, Japan: Japan Society of Mechanical Engineers, 1968.

**33 Downing, S. D.** and **Socie, D. F.** Simple rainflow counting algorithms. *Int. J. Fatigue*, 1982, **4**(1), 31–40.

**34 Kaufman, J. G.** *Properties of aluminum alloys: fatigue data and the effects of temperature, product form and processing*, 2008 (ASM International, Novelty, OH)

**35 Meggiolaro, M. A.** and **Castro, J. T. P.** Statistical evaluation of strain-life fatigue crack initiation predictions. *Int. J. Fatigue*, 2004, **26**, 463–476.

**36 Aghaie-Khafri, M.** and **Zargaran, A.** Low-cycle fatigue behaviour of AA2618-T61 forged disk. *Mater. Design*, 2010, **31**, 4104–4109.

## FIGURES

## TABLES

**Table 1.** Correlation coefficients for equation (4) [**23**].

| *d* [mm] | *a* | *b* |
|---|---|---|
| 2.2 | 1.15 | -0.23 |
| 4.1 | 1.34 | -0.41 |
| 5.8 | 1.48 | -0.56 |
| 8.9 | 1.57 | -0.7 |

**Table 2.** Thermal properties of the materials employed for the thermal analysis.

| Component | Material | Thermal conductivity [$W/m^2.K$] |
|---|---|---|
| Piston | Aluminum alloy AA2618 | 146 |
| Cylinder | Aluminum alloy AlSi10Mg | 155 |
| Engine block | Aluminum alloy AlSi7MgTi | 135 |
| Piston pin | Steel 33CrMoV12 | 39 |
| Con-rod | Steel 38NiCrMo4 | 52 |

**Table 3.** Main engine data.

| | | |
|---|---|---|
| Displacement | 1198 | $cm^3$ |
| Number of cylinders | 2 | |
| Bore | 106 | mm |
| Stroke | 67.9 | mm |
| Con-rod length | 124 | mm |
| Compression ratio | 12.8 | |
| Maximum revving speed | 11000 | rpm |

**Table 4.** Boundary conditions for the different load cases considered.

| Load case | Crank angle [°] | Acceleration [$m/s^2$] | Gas pressure [bar] |
|---|---|---|---|
| Maximum gas pressure | 373 | 56380 | 86.8 |
| Top dead centre during the beginning of the induction stroke | 0 | 58940 | 0.94 |
| Bottom dead centre | 540 | -31158 | 3.42 |
| Maximum lateral force during the expansion phase | 472 | -26868 | 8.19 |
| Maximum lateral force during the compression phase | 243 | -28617 | 1.74 |

**Table 5.** Mechanical properties of the materials employed for the mechanical analysis.

| Component | Material | Young's modulus [MPa] | Density [$kg/dm^3$] | Expansion coefficient [m/m.°C] |
|---|---|---|---|---|
| Piston | Aluminum alloy AA2618 | 74000 | 2.7 | $2.2x10^{-6}$ |
| Cylinder | Aluminum alloy AlSi10Mg | 74500 | 2.7 | $2.2x10^{-6}$ |
| Engine Block | Aluminum alloy AlSi7MgTi | 74000 | 2.7 | $2.2x10^{-6}$ |
| Piston Pin | Steel 33CrMoV12 | 210000 | 7.8 | $1.2x10^{-6}$ |
| Con-rod | Steel 38NiCrMo4 | 210000 | 7.8 | $1.1x10^{-6}$ |

**Table 6.** Piston material static parameters as functions of the temperature.

| Temperature | Young's modulus | "As forged" Chaboche parameters | | | "Fully aged" Chaboche parameters | | |
|---|---|---|---|---|---|---|---|
| T [°C] | *E* [MPa] | Yield stress, *R*s [MPa] | *K* | *γ* | Yield stress, *R*s [MPa] | *K* | *γ* |
| 20 | 74000 | 321 | 7403 | 45.3 | 321 | 7403 | 45.3 |
| 100 | 72000 | 311 | 5922 | 46.7 | 311 | 5922 | 46.7 |
| 200 | 68200 | 306 | 4313 | 48.6 | 228 | 2772 | 49.3 |
| 250 | 65500 | 237 | 650 | 53.2 | 111 | 244 | 53.5 |
| 300 | 62000 | 147 | 266 | 53.6 | 54 | 90 | 53.7 |

**Table 7.** Piston material fatigue parameters as functions of the temperature.

| Temperature [°C] | Fatigue limit [MPa] | Young's Modulus *E* [MPa] | Fatigue ductility coefficient $\varepsilon_f'$ | Fatigue ductility exponent *c* | Fatigue strength coefficient $\sigma_f'$ [MPa] | Fatigue strength exponent *b* |
|---|---|---|---|---|---|---|
| 20 | 123 | 74000 | 0.55 | -0.96 | 598 | -0.083 |
| 150 | 100 | 70000 | 0.55 | -0.96 | 638 | -0.097 |
| 200 | 82 | 68200 | 0.55 | -0.96 | 697 | -0.112 |
| 260 | 65 | 64000 | 0.55 | -0.96 | 729 | -0.1265 |
| 315 | 49 | 61000 | 0.55 | -0.96 | 682 | -0.1378 |